Electron Spin Resonance on the Border Between Para- and Ferromagnetism: Quantum versus Classical

V. A. Atsarkin & N. Noginova

Applied Magnetic Resonance

ISSN 0937-9347

Appl Magn Reson
DOI 10.1007/s00723-020-01213-1

Springer

Applied Magnetic Resonance
https://doi.org/10.1007/s00723-020-01213-1

Applied
Magnetic Resonance

REVIEW

Electron Spin Resonance on the Border Between Para- and Ferromagnetism: Quantum versus Classical

V. A. Atsarkin[1] · **N. Noginova**[2]

Received: 28 April 2020 / Revised: 9 June 2020

Abstract

The transition from para- to ferromagnetic behavior in magnetic systems can be considered to be a part of a general problem of the transition from quantum (one-particle) to classical (multiple-particle) behavior. Here we present a brief review of recent studies in electron magnetic resonance (EMR) and spin relaxation in situations which are at the borderline between paramagnetic and ferromagnetic cases. Most attention is paid to EMR in magnetic nanoparticles. It is shown that the giant spin model based on the quantum spin Hamiltonian can be successively applied for interpretation of the specific features observed in the experiment, such as a narrow spectral component and "forbidden" half-field resonances. Another example is the transformation of the level anticrossing typical for anisotropic EPR spectra of paramagnetic ions into the magnetic pseudoresonance (which manifests itself as a giant peak of radio-frequency absorption) observed in ferromagnets with axial anisotropy. Finally, an emergence and an intensification of the Bloch relaxation gradually replacing the Landau–Lifshit–Gilbert mechanism near the Curie point is clearly demonstrated in colossal magnetoresistance materials.

1 Introduction

A transition from paramagnetic to ferromagnetic behavior can be considered from general point of view as a transition from single-particle dynamics to many-particle thermodynamics, or, in the other words, from low-spin quantum mechanics to high-spin classical master equations.

This transition is illustrated in Fig. 1. Let us start from a single paramagnetic ion with effective spin S (for instance, $S = 3/2$) embedded in a diamagnetic solid matrix. This simple object is described by the spin-Hamiltonian quantum

✉ V. A. Atsarkin
atsarkin@cplire.ru

[1] Kotel'nikov Institute of Radio Engineering and Electronics of RAS, 125009 Moscow, Russia

[2] Norfolk State University, Norfolk, VA, USA

Published online: 28 August 2020

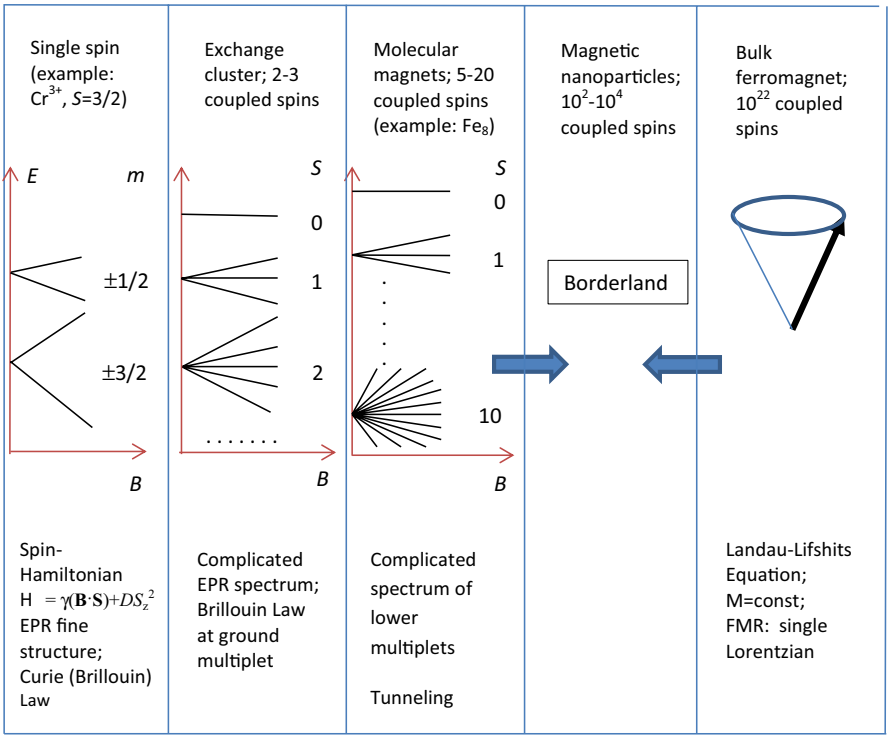

Fig. 1 The diagram illustrating the transition from para- to ferromagnetism upon increasing the number of interacting spins

formalism leading to the well-known energy level diagram in an external magnetic field **B** [1, 2]. The corresponding EPR spectrum has a simple fine structure reflecting the symmetry of the crystalline field. The transverse and longitudinal relaxation times, T_1 and T_2, are significantly different (as a rule, $T_1 \gg T_2$). As the next object, consider a spin cluster containing several spins S_i coupled by strong exchange interaction. The energy diagram consists of a number of spin multiplets. Assuming ferromagnetic exchange, the lowest spin multiplet has the maximum spin value $S = \sum S_i$. The EPR spectrum becomes more complicated featuring multiple lines. Passing further, we move to molecular nanomagnets (MNM) discovered in 1991–1993 [3, 4] and thoroughly investigated in subsequent years, see Refs. [5, 6] and references therein. A single molecule of such a material contains about 10–20 spins coupled by the ferromagnetic exchange interaction (typical examples are Fe_8 and Mn_{12} molecular clusters). At low temperatures it behaves as a classical ferromagnet, though some quantum properties are also observed, such as tunneling and quantum interference. Finally, at the right edge of the diagram, we have a bulk ferromagnet with, for example, 10^{20} exchange-coupled spins. Its FMR dynamics is described classically by the Landau–Lifshits–Gilbert equation as a precession of the total magnetic moment **M** in the effective field. The spectrum consists of a single FMR line, with the fixed ratio $T_1/T_2 = 1/2$ [7].

The blank spot between MNM and bulk ferromagnets ("Borderland" in Fig. 1) is occupied by magnetic nanoparticles (MNPs) containing hundreds or thousands exchange-coupled spins. The MNPs actually form a bridge between paramagnetism and ferromagnetism and are the first to be considered in this review.

The next topic discussed in this review is ferromagnetic pseudoresonance [8–12] which was recently interpreted in terms of anticrossing of quantum energy levels [13]. Finally, we discuss spin relaxation in colossal magnetoresistance materials at temperatures approaching Curie point, where the transition from the Landau–Lifshits–Gilbert model to Bloch relaxation has been shown both theoretically [14, 15] and experimentally [16, 17]. We review these three different cases, bearing in mind to draw attention to their common characteristic feature: the transition between classical and quantum behavior.

2 Electron Spin Resonance in Magnetic Nanoparticles: The Giant Spin Model

Magnetic nanoparticles have attracted considerable interest due to their unusual magnetic properties and many technological applications ranging from nanoscale engineering to medicine [18, 19]. Among publications on magnetic nanoparticles, there are a significant number of studies using electron magnetic resonance (EMR), see, for example, Refs. [20–25]. (Here we use the term EMR, leaving the terms EPR and FMR for the limiting cases). As a rule, the experimental samples were diluted suspensions (either solid or liquid) of nanoparticles, which are fabricated from ferromagnetic compounds and covered by protective layer to prevent aggregation.

The corresponding theory was developed [26–29], based on the classical description of ferromagnetic resonance (FMR) with account made for thermal reorientations of the magnetic moment. Thermal fluctuations play an important role in MNPs magnetic (superparamagnetic) behavior, when the magnetic energy $U_m=(\boldsymbol{\mu}\cdot\mathbf{B})$, as well as the anisotropy energy of a single MNP typically are of the order of k_BT. Here $\boldsymbol{\mu}$ is the magnetic moment of a single MNP and k_B is the Boltzmann constant. Using the rotary diffusion model, the effective averaging of the anisotropy field was predicted, leading to the narrowing of the EMR line with increasing temperature and decreasing the particle size. Qualitatively, these predictions agree with the experimental data; however, some features were observed that could not be explained in the framework of classical approach. First of all, this refers to an unusual EMR line shape which looks as a combination of wide and narrow components.

Typical examples are presented in Fig. 2a, b. The EMR spectra are taken at the X-band (the frequency $\omega/2\pi\sim 9.8$ GHz), for details see Refs. [30, 31]. In Fig. 2a, the spectra of maghemite (γ-Fe_2O_3) nanoparticles with the mean diameter $d=4.8$ nm randomly dispersed in solid polystyrene are shown at temperatures from 96 to 295 K [30]. As seen from the figure, the EMR spectra consist of broad and narrow components (the corresponding line-widths at 295 K are about 500 and 30 G, respectively). Upon decreasing temperature, the broad component shifts to lower fields, whereas its width increases. At the same time, the width and position (with g-factor about 2) of the narrow component remain constant, whereas its intensity decreases upon

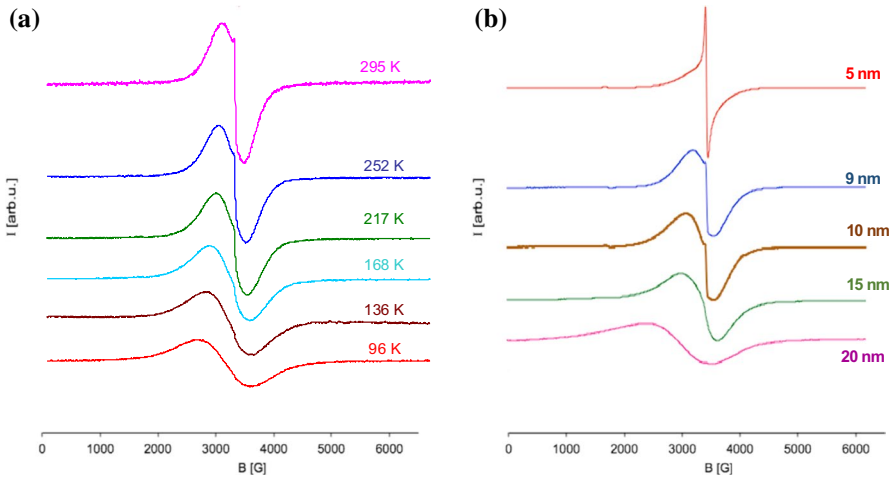

Fig. 2 **a** EMR spectra of the 4.8 nm γ-Fe_2O_3 nanoparticles dispersed in solid polystyrene at different temperatures (indicated at the curves [30]. **b** EMR spectra of the Fe_3O_4 nanoparticles of various size (indicated at the curves) at the room temperature [31]

cooling as $\exp(-E_a/k_BT)$ with $E_a/k_B \sim 850$ K; note that the activation energy is close to U_m.

In Fig. 2b, the size dependence of the EMR line shape is presented for randomly oriented Fe_3O_4 nanoparticles embedded in polystyrene (for details, see [31]). Again, the two-component spectra are observed, with the intensity of the narrow component increasing upon decreasing the particle size. Similar data were obtained for a wide variety of magnetic nanoparticles in different solid and liquid matrices [20, 21, 23, 32].

Another interesting feature observed in superparamagnetic nanoparticles, which is not readily described by the classical approach is an appearance of a weak EMR signal at the field $B_0/2$, where B_0 is the resonance field for the main line. Such half-field lines were observed firstly in maghemite MNPs [33] and then in various objects [31, 32, 34–36]; their corresponding temperature and size dependencies were studied as well. A typical example is shown in Fig. 3a. As seen, the half-field feature, similarly to the main line, consists of the narrow and broad components. Moreover, even weaker signals were detected in the fields B_0/k, $k = 3, 4$ [33, 36]; an example is shown in Fig. 3b.

In order to explain these unusual features in the EMR of small MNPs, a ''giant spin'' approach has been suggested [30, 37] considering the energy spectrum of a nanoparticle as a set of spin multiplets S, S-1,… As a simplifying approximation, it is assumed [30] that only the lowest multiplet corresponding to the sum $S = \sum S_i$ of the exchange coupled spins S_i is populated. In such a case, the EMR spectrum consists of contributions from the resonance transitions between separate energy levels E_m, corresponding to the projections m of the spin **S** onto the quantization axis (accounting for the directions of the external magnetic field **B** and the crystalline anisotropy). As a typical and a rather simple example, consider the case of the axial

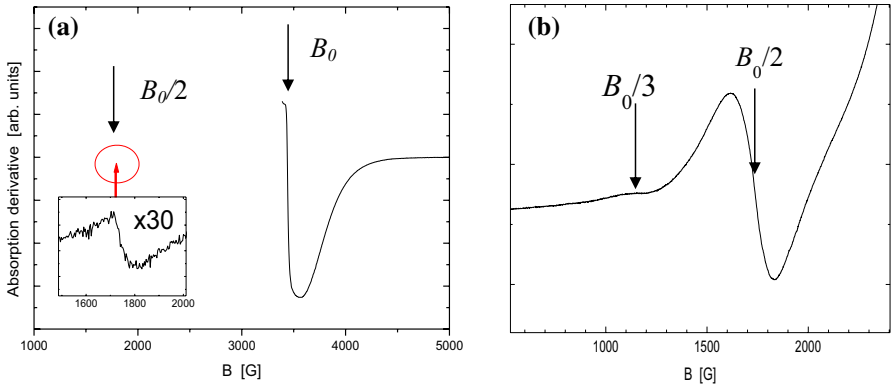

Fig. 3 "Forbidden" (B_0/k) resonances in the EMR spectra of the 4.8 nm maghemite nanoparticles dispersed in solid polystyrene (**a**) and in liquid toluene (**b**)

crystalline symmetry with the well-known spin Hamiltonian [1, 2] (in frequency units)

$$\frac{\hat{H}}{\hbar} = \gamma\left(\mathbf{B}\cdot\hat{\mathbf{S}}\right) + D\left(\hat{S}_Z^2 - \frac{S(S+1)}{3}\right), \tag{1}$$

where $\gamma<0$ is the electron gyromagnetic ratio, D is the axial anisotropy parameter (we suppose $D<0$), and Z axis is directed along the anisotropy axis $\mathbf{n_a}$. In the high-field approximation ($B \gg \mathrm{SD}/\gamma$), the resonance magnetic field for an allowed transition between the states m, $m+1$ reads:

$$B_0(m,\theta) = B_{00} + \frac{1}{\gamma}(2m+1)DP_2(\cos\theta), \tag{2}$$

where $B_{00} = \frac{\omega}{|\gamma|}$; $P_2(y)=(3y^2-1)/2$ is the Legendre polynomial, and θ is the angle which **B** makes with the anisotropy axis. A schematic sketch of the energy level diagram is shown in Fig. 4.

Due to the ferromagnetic exchange, the lowest (ground) level corresponds to $m=-S$, the highest state is $m=S$, and the central position is occupied by the doublet $\pm 1/2$ (at half-integer S) or by $m=0$ (at integer S). In order to get the resulting EMR spectrum, one must take into account the Boltzmann distribution of populations over $2S+1$ energy levels and the probabilities of the $2S$ allowed transitions between them. Finally, the integration should be performed over all orientations of the anisotropy axis due to random orientations of MNPs in diamagnetic matrix. Varying θ from 0 to $\pi/2$, the resonance field $B_{m,\theta}$ of a single transition, Eq. (2), covers the interval with the width of $1.5D|2m+1|/\gamma$ around B_0. The integration gives rise to a single and relatively broad line with the inhomogeneous width increasing with increasing $|2m+1|$. So the total contribution of the transitions with relatively high values of $|m|$ forms the broad component of the EMR line whereas the contributions of the central transitions (at m close to $\pm 1/2$ or 0) result in the narrow component. In the other words, the existence of the narrow peak is caused by insensitivity of the

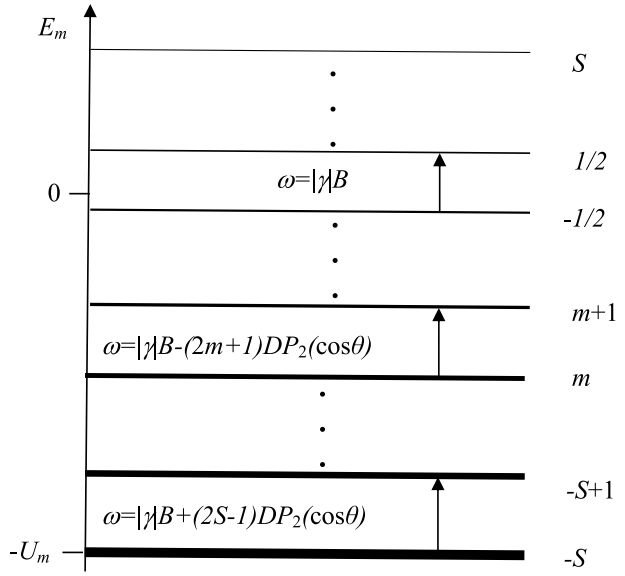

Fig. 4 Schematic energy diagram of the lowest spin multiplet corresponding to the spin Hamiltonian, Eq. (1). Quantum numbers m are shown on the right. Vertical series of dots indicate many intermediate levels. Arrows show allowed transitions with corresponding frequencies. The level population is indicated schematically by the line thickness

central transitions to the anisotropy fields (this is especially true for the $\pm 1/2$ transition obeying the Kramers theorem [1, 2]). Thus, the activation law observed in the temperature dependence of the narrow component intensity is clearly explained with the energy gap U_m between the ground state ($m=-S$) and high-lying energy levels with low values of $|m|$. On the other hand, an increase in Boltzmann population of the low energy levels with high $|m|$ values leads to the observed broadening of the wide component upon cooling.

The same giant spin model explains the weak additional EMR signals observed at B_0/k, $k=2, 3,\ldots$ These are the "forbidden" transitions with $\Delta m=k$, caused by mixing of neighboring quantum states and well-known in EPR spectroscopy [1, 2]. The mixing can be determined by both inter-MNP dipole–dipole interactions and a non-collinear with **B** anisotropy fields. In [32] the half-field EMR features were studied in detail using specially textured samples where randomly oriented nanoparticles were arranged in well aligned parallel chains in the porous alumina membrane matrix. The dipolar contribution was estimated quantitatively in the first order of the perturbation theory and demonstrated a good agreement with the experimental data. Model calculations have been also performed both analytically and numerically for different MNP systems in [31, 35, 36]. Some examples are shown in Fig. 5.

The transition to ferromagnetic limit is naturally achieved by decreasing the temperature to such an extent that only the lowest level ($m=-S$) is populated. The same can be done by increasing S, that is by growing the particle size. There is no phase transition as it would be in a bulk ferromagnet. Instead, the so-called spin blocking arises, which manifests itself in the difference between the magnetization behavior

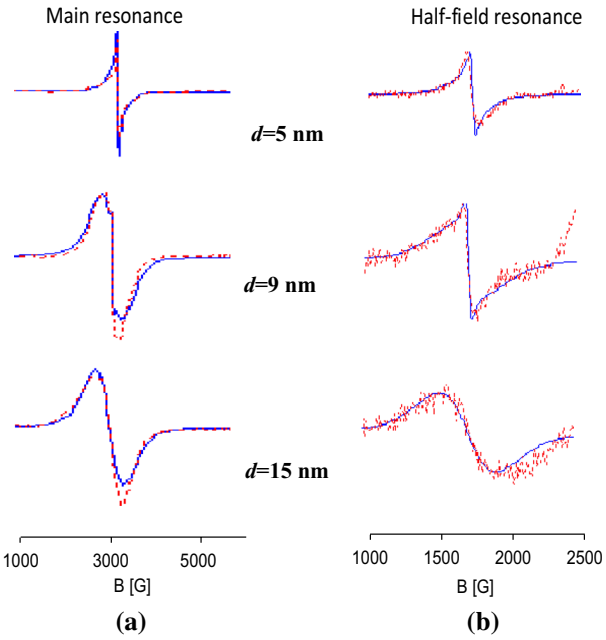

Fig. 5 The main (**a**) and half-field (**b**) resonances in Fe_3O_4 nanoparticles suspended in solid polymer: experiment (dotted) and fitting with the giant spin model (solid curves) [31]

upon field- and zero-field cooling, typical of superparamagnetism. For us, however, the most interesting is the transformation of the EMR spectrum. As seen from Eq. (2), at $m=-S$ (and $S\gg 1$) the resonance field coincides with the well-known expression for FMR in a ferromagnet with uniaxial magnetic anisotropy [9], supposing that $\boldsymbol{n_a}$ is the easy axis and the anisotropy field $B_a=2D(2S-1)/\gamma$.

Note that the role of the upper multiplets is ignored in our simplified giant spin model [30–34]. This is a substantial restriction of this approach. As a result, the description of the temperature and size dependencies of the EMR spectra remains rather phenomenological and includes some fitting parameters, such as the widths of individual quantum transitions [31].

It is of interest to compare the EMR and spin dynamics in MNPs with those in molecular nanomagnets. Unlike MNPs, the spin S of molecular nanomagnets is not very large. Besides, the magnetic molecules are commonly integrated in the crystal lattice and can be studied using the single-crystal samples. In this case, the EMR spectrum is well-resolved and consists of a number of separated lines corresponding to all possible transitions between the energy levels. Besides, some upper multiplets with lower S values can be also observed. For example, it was found that upper spin multiplets affects the EMR spectrum of a Ni_4 MNM [38], the relaxation rate (including tunneling) in a Mn_6 nanomagnet [39], etc.

Detailed analysis of the MNM-MNP transformation, including the role of the excited S multiplets, was thoroughly performed in a series of works published by

the group headed by Prof. Dante Gatteschi [35–37, 40, 41]. In Ref. [37], the energy spectra of upper multiplets are calculated for various space arrangements of spins forming MNM. It is demonstrated that, with S increasing, the EMR spectrum approaches that typical for magnetic nanoparticles. The MNM–MNP interplay has been further investigated in Refs. [35, 36, 40, 41]. In these studies, maghemite/magnetite MNPs were mineralized inside the internal cavity of protein cages; this method provides calibrated MNP sizes. Besides, the orientation dependence of the spectra similar to that in single crystals was obtained using a suspension of MNPs, frozen in the presence of an external magnetic field. The EMR spectra of MNPs have been studied at various temperatures and compared with the spectra of relatively large magnetic nanomagnets (Fe_{19} and Mn_{19}) with the well-established structure of energy levels. As a result, the quantum features of MNPs have been convincingly confirmed. Moreover, it has been shown that the excited spin multiplets contribute to the narrow spectral component and play role in thermal behavior of the spectra. Nevertheless, the convenience, clarity and usefulness of the simplified giant spin model as applied to MNPs have been confirmed beyond doubt.

3 From Level Anticrossing to Ferromagnetic Pseudoresonance

Recently, a strong narrow peak of the radio-frequency (r.f.) absorption (the imaginary part of dynamic magnetic susceptibility) has been observed and studied in ferromagnetic films with the in-plane uniaxial magnetic anisotropy [8–13]. This feature referred as "magnetic pseudoresonance" [11] occurs when the external magnetic field $\mathbf{B}$ is perpendicular to the easy anisotropy axis $\mathbf{n}_a$ and swept through the resonance value B_0 equal to the anisotropy field B_a. The FMR frequency at this specific point turns to zero [7], and the r.f. absorption is of relaxation nature with the Debye-type temperature dependence [11]. As shown in Ref. [13], this interesting phenomenon can be regarded as the classical limit of the well-known quantum effect of mutual repulsion (anticrossing) of energy levels related to the single-particle EPR spectra.

As in Sect. 1, here we start with a single paramagnetic center with spin $S=3/2$ subjected to an external magnetic field $\mathbf{B}$ and a crystalline field with the uniaxial symmetry, see the first column in Fig. 1. The energy spectrum of such a system is determined by the spin Hamiltonian, Eq. (1). Let us now suppose that $\mathbf{B}$ is perpendicular to the crystal axis. The corresponding energy diagram is shown in Fig. 6a, where the magnetic field B and energy E are normalized to the anisotropy field B_a and initial (zero-field) splitting $\Delta_0=|D|$ $(2S-1)$, respectively. Here we make use of the relation $|\gamma|B_a=\Delta_0$ suggested in the framework of the giant spin model [30] (see Sect. 2).

As seen in Fig. 6a, the frequency ω_{23} related to the gap between the levels 2 and 3 decreases upon increasing B and passes through a minimum denoted as Δ_{LAC} (marked by an arrow) at $B=B_{LAC}$. This is just the level anticrossing (LAC).

Let us follow the evolution of LAC upon increasing S up to the values typical of superparamagnetic objects. This implies thermal depopulation of all energy levels

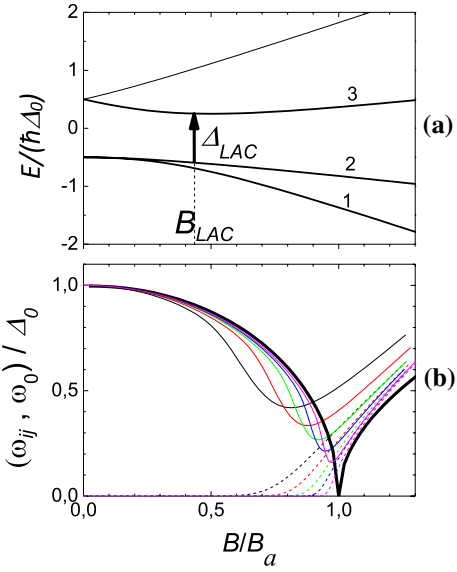

Fig. 6 **a** Energy diagram for a paramagnetic center with $S=3/2$ in the external magnetic field $\mathbf{B}\perp\mathbf{n}_a$. The level anticrossing (LAC) is indicated by an arrow. **b** The transition frequencies ω_{23} (thin solid lines) and ω_{12} (thin dashed lines) calculated for paramagnetic centers with $S=10$, 20, 40, 80 and 200 (from left to right) at $\mathbf{B}\perp\mathbf{n}_a$. The thick solid line shows the FMR frequency of a ferromagnetic film with uniaxial anisotropy at **B** directed along the in-plane hard axis

of the spin multiplet except for the lowest ones. The dependences of the frequencies ω_{12} and ω_{23} on the external magnetic field $\mathbf{B}\perp Z$ calculated with the spin Hamiltonian Eq. (1) at $S=10$, 20, 40, 80 and 200 are presented in Fig. 6b. When S increases, the value of Δ_{LAC} decreases progressively, whereas B_{LAC} approaches B_a.

When passing through the LAC point, the quantum states of the mutually repulsive levels are mixed and then interchanged. This leads to the possibility of tunneling, i.e. spontaneous change in orientation of magnetic moment characteristic of molecular nanomagnets. At the same time, a maximum in the magnetic susceptibility arises, being an early sign of the pseudoresonance.

Passing to the ferromagnetic limit ($S\to\infty$), one can expect that the FMR spectrum should be formed by the transition from the only populated lowest level to the next one, that is $(1, 2)\to 3$ at $B<B_{\mathrm{LAC}}$ and $1\to 2$ at $B>B_{\mathrm{LAC}}$. At $B=B_{\mathrm{LAC}}=B_a$, the FMR frequency tends to zero. This singularity along with a steep change in the quantum states of the involved levels at the LAC point should provide a strong increase of both static and dynamic magnetic susceptibility (magnetic pseudoresonance).

The same result can be obtained if one starts from the opposite side using the standard FMR approach. The field dependence of the FMR frequency ω_0 for a ferromagnetic sphere with the uniaxial anisotropy under conditions of $\mathbf{B}\perp\mathbf{n}_a$ was calculated using Landau–Lifshits equation [13]. The calculated curve is shown in Fig. 6b with the thick solid line. Note that the low-field and high-field branches of the $\omega_0(B)$ diagram correspond to the quantum transitions 2-3 and 1-2, respectively. Evidently, the $\omega_0(B)$ curve calculated with the classical FMR methods looks as the limit of the paramagnetic (quantum) description at $S\to\infty$; this confirms once again the validity of the giant spin approach (Sect. 2).

4 Change of the Relaxation Mechanism Near the Curie Point

The next example of the borderland between ferro- and para- magnetism is the change in the relaxation mechanism as a ferromagnet approaches the Curie point (T_C). At sufficiently low temperatures, all atomic spins of a ferromagnet are oriented in the same direction and form the total spin **S** (and corresponding ferromagnetic moment **M**) precessing around an effective field $\mathbf{H}_e$. This situation is reflected in the Landau–Lifshitz–Gilbert (LLG) equation which can be written in the form [7]

$$\frac{\partial \mathbf{M}}{\partial t} = -\gamma\left[\mathbf{M}\times\mathbf{H}_e\right] - \gamma\alpha\frac{\left[\mathbf{M}\times\left(\mathbf{M}\times\mathbf{H}_e\right)\right]}{M_0^2}, \tag{3}$$

where α is the Gilbert relaxation parameter and M_0 is saturated magnetization. According to Eq. (3), the length |**M**| of the vector **M** does not change during the relaxation process as well as under conditions of FMR excitation. In both cases, the total spin is only tilted from the direction of $\mathbf{H}_e\|\mathbf{z}$. By contrast, in the paramagnetic phase ($T > T_C$), spin dynamics is governed by Bloch equations [42] assuming different characteristic times, T_1 and T_2, for longitudinal and transverse spin relaxation. In this case, the magnitude |**M**| decreases when EPR is saturated by the resonant microwave field $B_1\exp(i\omega t)$. At the resonance ($B = B_0$), the relative decrement of the absolute magnetization value reads:

$$-\frac{\Delta|\mathbf{M}|}{M_0} \equiv s = \left(\gamma B_1\right)^2 T_2^2\left(a - \frac{1}{2}\right), \tag{4}$$

where $a = T_1/T_2$. At $a = 1/2$, the right side of Eq. (4) turns to zero, i.e. |**M**| remains constant as in the ferromagnetic case, Eq. (3). Thus, decreasing |**M**| under FMR conditions can be used as an indicator of the transition from ferromagnetic (LLG) to Bloch relaxation mechanism.

This opportunity has been implemented in the studies [16, 17] performed with the doped rare-earth manganite $La_{2/3}Sr_{1/3}MnO_3$ (LSMO). This material is a metal ferromagnet with Curie temperature $T_C \cong 350$ K convenient for experimental work. But even more important is a relatively strong dependence of electrical resistance R on the external magnetic field B (the colossal magnetoresistance effect, CMR) typical for rare-earth manganites [43]. According to the double-exchange model [44, 45], this effect is due to incomplete alignment of spins of the manganese ions, which hinders the electron jumps. As a result, the electrical resistivity decreases with increasing |**M**|, providing one an opportunity to monitor changes in |**M**| under the FMR pumping with the resistance measurements.

The experiments were performed with thin epitaxial films of LSMO (with the thickness of 50–100 nm) grown on the $NdGaO_3$ single-crystal substrates. The details are presented in Ref. [46]. Routine R measurements were performed with the samples placed into a rectangular cavity and subjected to the microwave pumping ($\omega/2\pi \sim 9.5$ GHz) with the power P of 100–500 mW ($B_1 \sim 0.5$ G). In order to increase sensitivity, the microwave power was modulated with frequency of 100 kHz with consequent lock-in detection and accumulation. For the

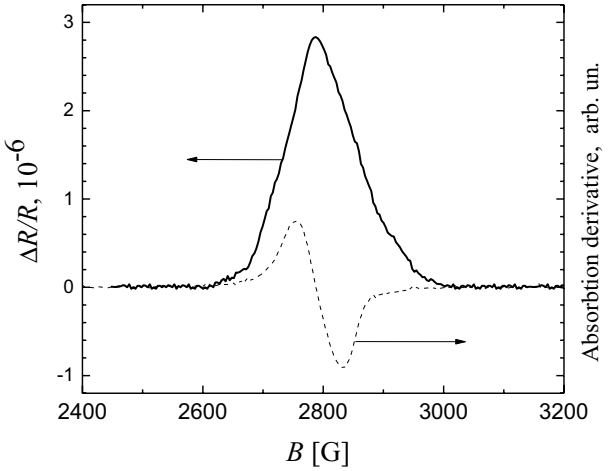

Fig. 7 Left scale, solid curve: relative change in electrical resistance measured in the LSMO film under microwave pumping ($P = 116$ mW, $T = 331$ K) when sweeping magnetic field through the FMR conditions. The dotted curve shows the commonly detected FMR line [17]

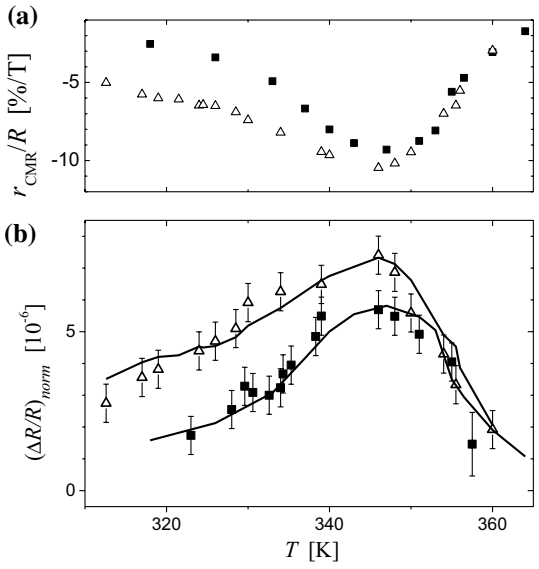

Fig. 8 Temperature dependences of relative magnetoresistance (**a**) and normalized resonant resistance change (**b**) in two LSMO films [17]. Points are the experimental data, the solid curves are calculated with Eq. (6)

experimental details see Refs. [16, 17]. The $R(B)$ plots were recorded by sweeping the magnetic field across its resonant value B_0. Typical experimental results are presented in Fig. 7, where, for comparison, the FMR line recorded in usual way is also shown. As seen, this technique may be considered as an electrical detection of magnetic resonance (EDMR). The most interesting is the evolution of this effect when the temperature approaches $T_C = 348$ K and then passes to

the paramagnetic region. In Fig. 8b, the relative change in the film resistance, $(\Delta R/R)_{\text{norm}}$, is plotted as the function of temperature for two LSMO samples [17]. The data correspond to the resonance conditions ($B = B_0$) and are normalized to account for changes in the EMR line width (δB). For comparison, the temperature dependence of the differential CMR, r_{CMR}/R, where $r_{\text{CMR}} = [R(B=0) - R(B)]/B$, is shown in Fig. 8a.

The correlation between the EDMR and CMR effects is obvious, thus supporting our interpretation. Moreover, it turned out that a quantitative comparison is possible based on the so-called Landau–Lifshits–Bloch (LLB) equation that is supposed to describe spin dynamics at the transition from ferro- to paramagnetism [14, 15]. Not far from T_{C} it can be written as

$$\frac{\partial \mathbf{M}}{\partial t} = -\gamma\left[\mathbf{M}\times\mathbf{H}_{\text{e}}\right] + \gamma\alpha_{//}\frac{(\mathbf{M}\cdot\mathbf{H}_{\text{e}})\mathbf{M}}{M^2} - \gamma\alpha_{\perp}\frac{\left[\mathbf{M}\times\left[\mathbf{M}\times\mathbf{H}_{e}\right]\right]}{M^2}, \tag{5}$$

where $\alpha_{//}$ and $\alpha_{\perp}$ are relaxation parameters for longitudinal and transverse relaxation rates, respectively. Using the expressions for these quantities [15] and accounting for the CMR effect, one can get the formula for the EDMR effect at resonance [17]:

$$\left(\frac{\Delta R}{R}\right)_{\text{norm}} = -2\gamma\frac{T_{1\text{abs}}}{\chi_{\text{abs}}}\cdot\frac{r_{\text{CMR}}B_1^2}{R}, \tag{6}$$

where $T_{1\text{abs}}$ and χ_{abs} are correspondingly the relaxation time and susceptibility along the **M** direction. In order to compare the model with the experiment, the values of r_{CMR}, B_1, R and χ_{abs} were measured directly, and the only fitting parameter was $T_{1\text{abs}}$. The best-fit curves for two samples are plotted in Fig. 8b, showing an excellent agreement with the experimental data. Note that the best-fit values of $T_{1\text{abs}}$ (~2 ns at $T = T_{\text{C}}$) turned out to be close to T_1 values measured experimentally in various manganites in the vicinity of T_{C} [47, 48]. Thus, the data shown in Fig. 7b may be perceived as a symbolic image of the bridge between ferro- and paramagnetic lands.

In conclusion, various aspects are investigated related to the specifics of magnetic resonance spectra and spin dynamics at the border between para- and ferromagnetism. The transition is traced from the quantum approach adequate for the description of one or several objects, to multi-particle systems described by the classical thermodynamics. A prime example of such a transition is evolution of quantum features (such as the narrow spectral component and B_0/k resonances) observed in EMR spectra of magnetic nanoparticles. The giant spin model, which replaces the real energy spectrum of a nanoparticle with the lowest spin multiplet, can describe the behavior of such borderline systems in a broad range of temperatures and particle sizes on the way from para- to ferromagnetism. Another impressive example is the transition from the level anticrossing typical for anisotropic EPR spectra into the FMR singularity (pseudoresonance) at $S \to \infty$. Finally, the emergence and gradual increase of Bloch-type relaxation mechanism in a ferromagnet when approaching and then crossing T_{C} was clearly demonstrated with the EMR detection technique based on the colossal magnetoresistance effect. The key factor that determines the transition from Gilbert to Bloch

relaxation mechanism is the increase in thermal fluctuations in the orientation of **M**. In fact, this phenomenon underlies all the situations discussed above.

The considered examples once again demonstrate unique capabilities of magnetic resonance in studying the most fundamental physical problems, such as the interplay between quantum and classical approaches.

Acknowledgements The authors thank V.V. Demidov and A.E. Mefed for their help at different stages of this study. For one of the authors (V.A. A.), this work was carried out within the framework of the state task. N.N. would like to acknowledge support from NSF #1830886, AFOSR FA9550-18-1-0417 and DoD #W911NF1810472 grants.

References

1. S.A. Al'tshuler, B.M. Kozyrev, *Electron Paramagnetic Resonance in Compounds of Transition Elements* (Willey, London, 1974)
2. A. Abragam, B. Bleaney, *Electron Paramagnetic Resonance of Transition Ions* (Clarendon Press, Oxford, 1970)
3. A. Caneschi, D. Gatteschi, R. Sessoli, A.L. Barra, L.C. Brunel, M. Guillot, J. Am. Chem. Soc. **113**, 5873 (1991)
4. R. Sessoli, D. Gatteschi, A. Caneschi, M.A. Novak, Nature **365**, 141 (1993)
5. D. Gatteschi, R. Sessoli, J. Villain, *Molecular Nanomagnets* (Oxford University Press, Oxford, 2006)
6. E.J.L. McInnes, *Spectroscopy of Single-molecule Magnets*, ed. by R. E. P. Winpenny (Springer, Berlin, 2006)
7. G. Gurevich, G.A. Melkov, *Magnetization Oscillations and Waves* (CRC Press, Boca Raton, 1996)
8. B.A. Belyaev, A.V. Izotov, S.Y. Kiparisov, Pis'ma ZhETF **74**, 248 (2001). **(JETP Lett. 74, 226 (2001))**
9. T.M. Vasilevskaya, D.I. Sementsov, Zh. Eksp. Teor. Fiz **137**, 861 (2010). **(JETP 110, 754 (2010))**
10. V.V. Demidov, I.V. Borisenko, A.A. Klimov, G.A. Ovsyannikov, A.M. Petrzhik, S.A. Nikitov, Zh. Eksp. Teor. Fiz. **139**, 943 (2011). **(JETP 112 825 (2011))**
11. V.A. Atsarkin, V.V. Demidov, A.E. Mefed, V.Yu. Nagorkin, Appl. Magn. Reson. **45**, 809 (2014)
12. V.V. Demidov, A.E. Mefed, Zh. Tekh. Fiz. **89**(1), 72 (2019). **(Technical Physics 64 (1), 64 (2019))**
13. V.A. Atsarkin, V.V. Demidov, V.Yu. Nagorkin, J. Phys. Commun. **2**, 035034 (2018)
14. D.A. Garanin, Phys. Rev. B **55**, 3050 (1997)
15. O. Chubykalo-Fesenko, U. Nowak, R.W. Chantrell, D.A. Garanin, Phys. Rev. B **74**, 094436 (2006)
16. V.A. Atsarkin, V.V. Demidov, L.V. Levkin, A.M. Petrzhik, Phys. Rev. B **82**, 144414 (2010)
17. V.A. Atsarkin, V.V. Demidov, Zh. Exper. Teor. Fiz. **143**(1), 109 (2013). **(JETP 116 (1), 95 (2013))**
18. T. Shinjo, ed., *Nanomagnetism and Spintronics* (Elsevier, Amsterdam, 2009)
19. W. Andrä and H. Nowak, eds., *Magnetism in Medicine: A Handbook* (Wiley-VCH, Weinheim Germany, 2007)
20. F. Gazeau, V. Shilov, J.C. Bacri, E. Dubois, F. Gendron, R. Perzynski, YuL Raikher, V.I. Stepanov, J. Magn. Magn. Mater. **202**, 535 (1999)
21. R. Berger, J. Kliava, J.-C. Bissey, V. Baietto, J. Appl. Phys. **87**, 7389 (2000)
22. YuA Koksharov, S.P. Gubin, I.D. Kosobudsky, GYu. Yurkov, D.A. Pankratov, L.A. Ponomarenko, M.G. Mikheev, M. Beltran, Y. Khodorkovsky, A.M. Tishin, Phys. Rev. B **63**, 012407 (2000)
23. R.J. Usselman, M.T. Klem, M. Allen, E.D. Walter, K. Gilmore, T. Douglas, M. Young, Y. Idzerda, D.J. Singel, J. Appl. Phys. **97**, 10M523 (2005)
24. C. Antoniak, J. Linder, M. Farle, Europhys. Lett. **70**, 250 (2005)
25. N.E. Domracheva, V.E. Vorobeva, M.S. Gruzdev, Y.N. Shvachko, D.V. Starichenko, Inorg. Chim. Acta **465**, 38 (2017)
26. Y.L. Raikher, V.I. Stepanov, Sov. Phys. JETP **75**, 764 (1992)
27. YuL Raikher, V.I. Stepanov, Phys. Rev. B **50**, 6250 (1994)
28. E. de Biasi, C.A. Ramos, R.D. Zysler, J. Magn. Magn. Mater. **262**, 235 (2003)

29. I.S. Poperechny, YuL Raikher, Phys. Rev. B **93**, 014441 (2016)
30. N. Noginova, F. Chen, T. Weaver, E.P. Giannelis, A.B. Bourlinos, V.A. Atsarkin, J. Phys.: Condens. Matter **19**, 246208 (2007)
31. N. Noginova, B. Bates, V.A. Atsarkin, Appl. Magn. Reson. **47**(8), 937 (2016)
32. N. Noginova, Yu. Barnakov, A. Radocea, V.A. Atsarkin, J. Magn. Magn. Mater. **323**, 2264 (2011)
33. N. Noginova, T. Weaver, E.P. Giannelis, A.B. Bourlinos, V.A. Atsarkin, V.V. Demidov, Phys. Rev. B **77**, 014403 (2008)
34. M.M. Noginov, N. Noginova, O. Amponsah, R. Bah, R. Rakhimov, V.A. Atsarkin, J. Magn. Magn. Mater. **320**, 2228 (2008)
35. L. Castelli, M. Fittipaldi, A.K. Powell, D. Gatteschi, L. Sorace, Dalton Trans. **40**, 8145 (2011)
36. M. Fittipaldi, R. Mercatelli, S. Sottini, P. Ceci, E. Falvo, D. Gatteschi, Phys. Chem. Chem. Phys. **18**, 3591 (2016)
37. M. Fittipaldi, L. Sorace, A.L. Barra, C. Sangregorio, R. Sessoli, D. Gatteschi, Phys. Chem. Chem. Phys. **11**, 6555 (2009)
38. A. Wilson, J. Lawrence, E.-C. Yang, M. Nakano, D.N. Hendrickson, S. Hill, Phys. Rev. B **74**, 140403(R) (2006)
39. S. Carretta, T. Guidi, P. Santini, G. Amoretti, O. Pieper, B. Lake, J. van Slageren, F. El Hallak, W. Wernsdorfer, H. Mutka, M. Russina, C.J. Milios, E.K. Brechin, Phys. Rev. Lett. **100**, 157203 (2008)
40. M. Fittipaldi, C. Innocenti, P. Ceci, C. Sangregorio, L. Castelli, L. Sorace, D. Gatteschi, Phys. Rev. B **83**, 104409 (2011)
41. A. Cini, P. Ceci, E. Falvo, D. Gatteschi, M. Fittipaldi, Z. Phys. Chem. **231**(4), 745 (2017)
42. A. Abragam, *The Principles of Nuclear Magnetism* (Clarendon Press, Oxford, 1961)
43. M.B. Salamon, M. Jaime, Rev. Mod. Phys. **73**, 583 (2001)
44. C. Zener, Phys. Rev. **81**, 440 (1951). **(82, 403 (1951))**
45. P.W. Anderson, H. Hasegawa, Phys. Rev. **100**, 675 (1955)
46. G.A. Ovsyannikov, A.M. Petrzhik, I.V. Borisenko, A.A. Klimov, YuA Ignatov, V.V. Demidov, S.A. Nikitov, Zh. Eksp. Teor. Fiz. **135**, 56 (2009). **(JETP 108, 48 (2009))**
47. V.A. Atsarkin, V.V. Demidov, G.A. Vasneva, K. Conder, Phys. Rev. B **63**, 092405 (2001)
48. V.A. Atsarkin, V.V. Demidov, F. Simon, R. Gaal, Y. Moritomo, K. Conder, A. Janossy, L. Forro, J. Magn. Magn. Mater. **258–259**, 256 (2003)